EOS

EOS, TRANSACTIONS, AMERICAN GEOPHYSICAL UNION

New Insight Into the Disappearing Arctic Sea Ice

PAGES 509–511

The dramatic loss of Arctic sea ice is ringing alarm bells in the minds of climate scientists, policy makers, and the public. The extent of perennial sea ice—ice that has survived a summer melt season—has declined 20% since the mid-1970s [*Stroeve et al.*, 2005]. Its retreat varies regionally, driven by changes in winds and heating from the atmosphere and ocean.

Limited data have hampered attempts to identify which culprits are to blame, but new satellite-derived information provides insight into the drivers of change. A clear message emerges. The location of the summer ice edge is strongly correlated to variability in longwave (infrared) energy emitted by the atmosphere (downward longwave flux; DLF), particularly during the most recent decade when losses have been most rapid. Increasing DLF, in turn, appears to be driven by more clouds and water vapor in spring over the Arctic.

Reduced ice in spring and summer is important to the climate system because the timing coincides with strongest insolation, of which ice is an excellent reflector. If enough ice is lost to allow sufficient extra heat into the Arctic Ocean, such that some can remain through the winter and reduce ice thickness the following spring, the so-called ice-albedo feedback will accelerate the loss of ice [e.g., *Serreze and Francis*, 2006]. Recent accelerating declines in summer and winter ice extent [*Meier et al.*, 2005] suggest this threshold has been crossed.

Integrated anomalies in winds and heating over months prior to maximum ice retreat are likely the primary drivers of ice edge location. New satellite products—downward longwave and shortwave fluxes (DLF, DSF), zonal and meridional winds (U,V), and temperature advection (ADV)—provide tools to investigate causes for ice loss.

New Satellite Information

In this study, the edge of compact sea ice, defined here as the southernmost latitude of

50% concentration from daily passive microwave satellite data, is identified in six peripheral seas (Figure 1a). The distance from the edge (averaged over six degrees of longitude) southward to a fixed position is measured, and the date of maximum annual ice retreat establishes the reference point from which forcing anomalies are integrated backward in time. Maximum ice retreat anomalies (MIAs) are calculated by subtracting the position for each year from the 26-year mean position in that region.

Time series of anomalies for each forcing parameter are calculated from daily-mean values within 400 kilometers of the mean MIAs. Anomalies for 10-day intervals are normalized by their standard deviation then integrated backward in time for 90 days beginning at the date of maximum ice retreat. Daily mean DLF, ADV (1000 to 850 hectopascal layer), and near-surface winds over the Arctic from 1979 to 2004 are

derived from Television Infrared Observation Satellites (TIROS) Operational Vertical Sounder (TOVS) [*Francis et al.*, 2005]. Surface solar fluxes are obtained from the extended advanced very high resolution radiometer (AVHRR) Polar Pathfinder (APP-x) project [*Wang and Key*, 2005].

What Drives Ice-Edge Variability?

Regional time series of MIAs (Figure 1b) reveal large interannual variability everywhere, with statistically significant (>99% confidence) trends in the Chukchi and Beaufort seas of 168 and 113 kilometers per decade, respectively. Relationships between MIAs and individual forcing anomalies are predominantly linear; DLF anomalies are consistently positively correlated with ice retreat, while DSF anomalies are consistently negatively correlated. This implies that variability in solar fluxes, owing primarily to varying cloud opacity, is overwhelmed by opposing changes in emitted longwave radiation. Because DSF anomalies apparently do not drive MIAs, they are excluded from further analysis.

The relative contributions of anomalies in forcing parameters to ice edge variability is
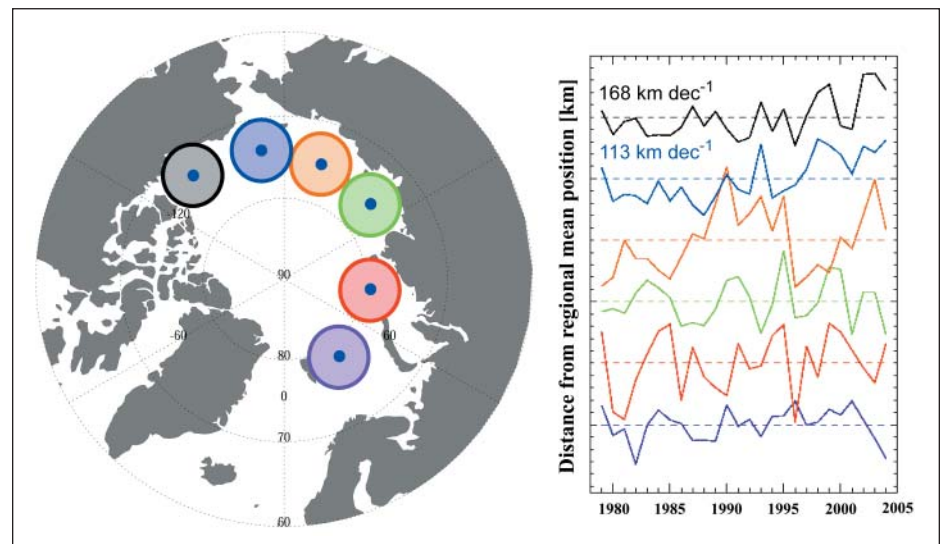

Fig. 1. (a) Approximate locations of mean perennial ice edge locations in six regions (solid blue circles), and 400-kilometer-radius areas in which forcing anomalies are determined (counterclockwise from lower right: Barents (purple), Kara (red), Laptev (green), East Siberian (orange), Chukchi (blue), Beaufort (gray)). (b) Time series of anomalies in northernmost location of perennial ice edge. Dashed lines indicate zero anomaly relative to the 1979–2004 mean; ticks on the y-axis denote 100 kilometers. Statistically significant trends, with >99% confidence determined by standard F-test, are found in the Beaufort and Chukchi seas, as indicated by the listed rates of change (in kilometers per decade; km dec⁻¹)

J. A. FRANCIS AND E. HUNTER

investigated with multiple regression analysis, as tests for the applicability of this approach revealed no violations of regression theory. Histograms in Figure 2 depict the variance in MIAs attributable to anomalies in each forcing parameter, integrated from zero to 80 days before the date of maximum ice retreat. The bar height indicates the total variance, while colored sections denote statistically significant (>90%) contributions by each parameter. The predominance of green indicates that DLF is by far the primary driver of variability in MIAs in all regions. In the Laptev and East Siberian seas, less total variance is accounted for, suggesting that ocean influences, river discharge, and/or nonlinear effects also may affect ice edge position [*Steele and Ermold,* 2004; *Polyakov et al.,* 2005].

A comparison with an analysis using detrended anomalies reveals that half of the variance in the Chukchi and Beaufort seas is due to trends, but elsewhere little difference is observed. In the Barents and Kara seas, ADV and southerly (from the south) wind anomalies also play significant roles in controlling ice edge position, particularly anomalies earlier in the melt season. Spring forcing appears dominant in the Beaufort Sea, consistent with findings by *Drobot and Maslanik* [2003].

The apparent acceleration of ice loss during the past decade and pan-Arctic thinning since the 1980s [*Rigor and Wallace,* 2004] raise the question: Were the relative roles of ice-edge drivers different in the 1980s compared with later years of rapid retreat? The relative importance of forcings before and after 1991 is presented in Figure 3 for two illustrative regions: the Barents and Chukchi seas (results are insensitive to year of split).

The differences are striking. In the Barents Sea, DLF and southerly wind anomalies dominate MIAs during the 1980s. After 1991, the total attributable variance is substantially reduced and ADV anomalies are most important, perhaps driven by the generally positive phase of the Arctic Oscillation (AO) during the latter interval [*Rigor and Wallace*, 2004], which enhances the northward transport of warm, moist air and Atlantic water. In the Chukchi Sea, variance in MIAs is dominated by southerly wind anomalies in the 1980s, then by DLF in the later period. This is consistent with evidence that ice thickness decreased markedly here in the last decade [e.g., *Rothrock and Zhang*, 2005]. Thin ice requires less energy to remove it, thus its extent is more vulnerable to anomalies in the surface energy balance.
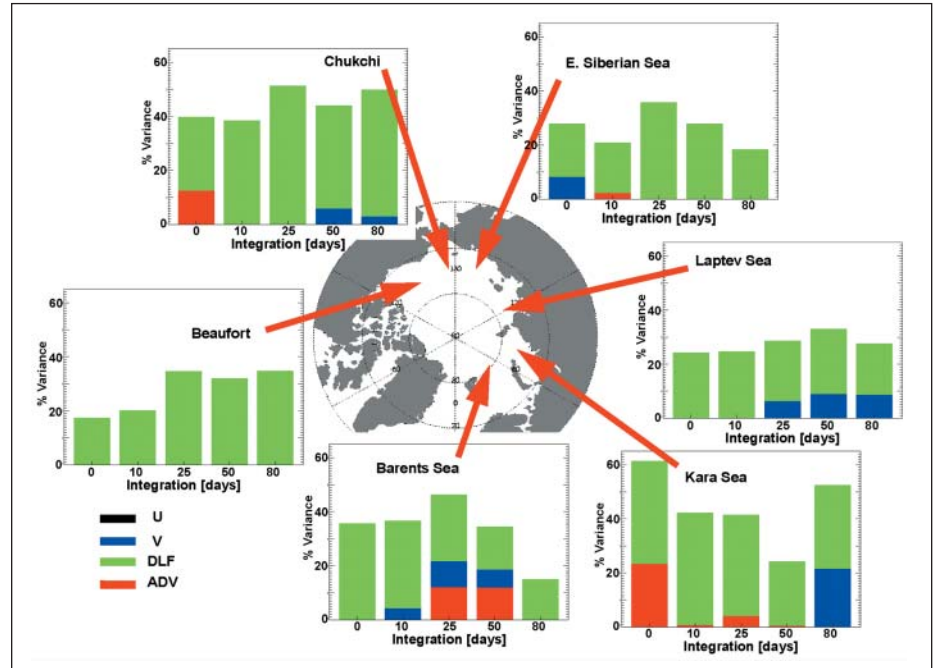

Fig. 2. Histograms exhibiting the total variance in the perennial ice edge attributable to anomalies in forcing parameters, integrated backward in time from the date of maximum ice retreat. Colors denote the portion contributed by each forcing parameter.
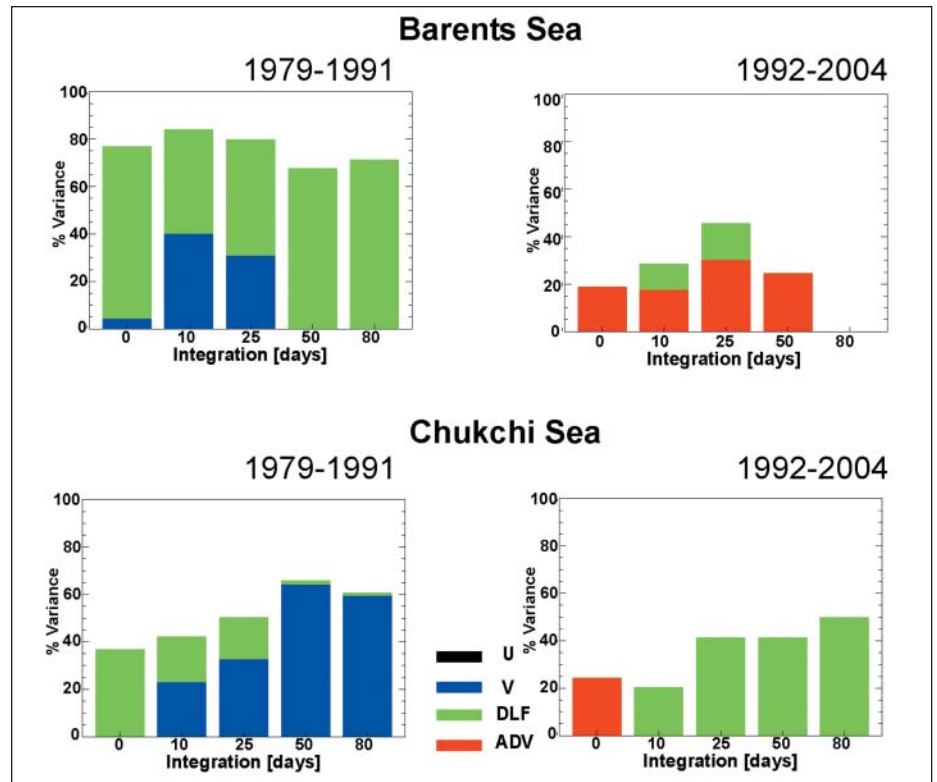

Fig. 3. Histograms similar to those in Figure 2 but specific to the Beaufort and Chukchi seas, with time series split into two intervals: 1979–1991 and 1992–2004.

What Drives the Infrared Flux?

In addition to warming and increased clouds, more abundant liquid-water-containing clouds [*Zuidema et al.*, 2005] and increased atmospheric water vapor content [*Wang and Key,* 2005] also appear to be influential. Trends in satellite-derived observations (Table 1) likely are caused by a combination of increased moisture transport from lower latitudes [*Groves and Francis,* 2002], as well as by evaporation from additional ice-free areas and from an earlier start to the melt season [*Belchansky et al.*, 2003]. These changes constitute a positive feedback to Arctic warming, augmenting the much anticipated ice-albedo feedback.

Thinner ice cover remaining after the period of positive AO during the late 1980s and early 1990s may have left the Arctic more vulnerable to changes in its surface energy balance. Results from this study support this explanation for a reduced sensitivity of ice extent to the AO. Since the late 1990s, the AO index has been in a near-neutral phase while ice

extent has continued to decline, suggesting that anomalies in the surface energy balance, rather than wind anomalies, now have a greater influence on ice extent. Increased temperatures, cloud amount, and water vapor—consistent with global-scale anthropogenic effects—enhance the atmosphere's infrared emission, which reduces the thickness as well as the extent of the thinner ice cover. As greenhouse gases continue to increase, it is plausible, perhaps likely, that this trajectory will continue. Simulations of the 21st century by global climate models project further loss of perennial ice, and this study points to an ice-infrared feedback as being a primary driver.

Table 1. Approximate Summer (JJA) Linear Trends (% of summer mean per decade) in Parameters That Directly Affect DLF: Cloud Liquid/Ice Water Path (LWP), Temperature in 1000-to-700 hPa Layer (T_{trop}), Precipitable Water (PW), Cloud Fraction (CLD), and Cloud-Base Height (CB)[a].

	Barents	Kara	Laptev	Siberian	Chukchi	Beaufort	Pan-Arctic
DLF	*1.3*	*1.9*	*1.7*	*2.0*	*2.4*	*2.0*	++
LWP	*65.5*	*60.6*	*51.5*	*63.8*	*88.0*	*73.4*	n/a
T_{trop}	*3.0*	*2.4*	*2.6*	*4.2*	*4.0*	*3.2*	++
PW	*3.0*	1.2	0.9	3.1	2.9	1.1	+
CLD	0.5	*2.6*	*1.7*	2.0	*3.2*	*4.2*	++
CB[b]	*1.1*	*1.4*	*2.1*	*2.3*	*2.5*	*2.2*	n/a

[a]Positive values denote higher cloud bases.
[b]Regional trends in bold italics are significant with >90% confidence according to a standard F-test. Signs of pan-Arctic trends are derived from AVHRR retrievals [*Wang and Key*, 2005]; significance >90% is indicated by double plus signs.

References

Belchansky, G. I., D. C. Douglas, and N. G. Platonov (2003), Duration of the Arctic sea ice melt sea son: Regional and interannual variability, 1979–2001, *J. Clim., 17*, 67–80.

Drobot, S. D. and J. A. Maslanik (2003), Interannual variability in summer Beaufort sea ice conditions: Relationship to spring and summer surface and atmospheric variability, *J. Geophys. Res., 108*, 3233, doi:10.1029/2002JC001537.

Francis, J. A., E. Hunter, J. Key, and X. Wang (2005), Clues to variability in Arctic minimum sea ice extent, *Geophys. Res. Lett., 32*, L21501, doi:10.1029/2005GL024376.

Groves, D. G. and J. A. Francis (2002), Variability of the Arctic atmospheric moisture budget from TOVS satellite data, *J. Geophys. Res., 107*(D24), 98–112.

Meier, W., J. Stoeve, F. Fetterer, and K. Knowles (2005), Reductions in Arctic Sea Ice Cover No Longer Limited to Summer, *Eos Trans. AGU, 86*(36), 326.

Polyakov, V., et al. (2005), One more step toward a warmer Arctic, *Geophys. Res. Lett., 32*, L17605, doi:10.1029/2005GL023740.

Rigor, I. G. and J. M. Wallace (2004), Variations in the age of Arctic sea-ice and summer sea-ice extent, *Geophys. Res. Lett., 31*, L09401, doi:10.1029/2004GL019492.

Rothrock, D. A. and J. Zhang (2005), Arctic Ocean sea ice volume: What explains its recent depletion?, *J. Geophys. Res., 110*, C01002, doi:10.1029/2004JC002282.

Serreze, M. C. and J. A. Francis (2006), The Arctic amplification debate, *Clim. Change*, doi:10.1007/s10584-005-9017-y.

Steele, M., and W. Ermold (2004), Salinity trends on the Siberian shelves, *Geophys. Res. Lett., 31*, L24308, doi:10.1029/2004GL021302.

Stroeve, J. C., M. C. Serreze, F. Fetterer, T. Arbetter, W. Meier, J. Maslanik, and K. Knowles (2005), Tracking the Arctic's shrinking ice cover: Another extreme minimum in 2004, *Geophys. Res. Lett., 32*, L04501, doi:10.1029/2004GL021810.

Wang, X., and J. R. Key, (2005), Arctic surface, cloud, and radiation properties based on the AVHRR Polar Pathfinder dataset: Part II. Recent trends, *J. Clim., 18*, 2575–2593.

Zuidema, P., B. Baker, Y. Han, J. Intrieri, J. Key, P. Lawson, S. Matrosov, M. Shupe, R. Stone, and T. Uttal (2005), An Arctic springtime mixed-phase cloudy boundary layer observed during SHEBA, *J. Atmos. Sci., 62*, 160–176.

Author Information

Jennifer A. Francis and Elias Hunter, Institute of Marine and Coastal Sciences, Rutgers University, New Brunswick, N.J.; E-mail: francis@imcs.rutgers.edu

Tracking Climate Forcing: The Annual Greenhouse Gas Index

Global monitoring of atmospheric greenhouse gases, in particular carbon dioxide (CO_2), has been a goal of the U.S. government for over 30 years. The monitoring program evolved into high-precision measurements of global, long-lived greenhouse gases that are used to calculate changes in radiative climate forcing. The change in global radiative forcing caused by increases in atmospheric abundances of long-lived greenhouse gases has been used to define the Annual Greenhouse Gas Index [*Hofmann et al.*, 2006].

This article presents a brief history of global greenhouse gas measurements of the U.S. National Oceanic and Atmospheric Administration (NOAA), and how these data are being made accessible and user-friendly.

Much of this work derived its impetus from Charles (Dave) Keeling's pioneering measurements of atmospheric CO_2 in Antarctica and at Mauna Loa Observatory in Hawaii during the International Geophysical Year (1957–1958). Beginning with U.S. Navy support in 1957 and later supported by the U.S. National Science Foundation and NOAA, Keeling's measurements of CO_2 from air samples collected at the South Pole began the longest record of CO_2 from any one location. At Mauna Loa Observatory, the U.S. Weather Bureau supported the installation and operation of a commercial infrared gas analyzer provided by Keeling, which began recording CO_2 in March 1958, and resulted in the beginning of the longest continuous CO_2 record (see *Keeling* [1998] for biographical information).

It was Keeling's initiative and expertise that got the measurements started, and field support through the federal government that continued the record for nearly 50 years under successive agencies responsible for U.S. weather-related activities—the Environmental Science Services Administration in 1965, and NOAA in 1970. Throughout this time, the Mauna Loa Observatory grew and expanded; Figure 1 shows the Mauna Loa Observatory at its dedication on 28 June 1956 and 50 years later.

Already in the late 1960s, predecessors of the NOAA Earth System Research Laboratory in Boulder, Colo., began the expansion of the global network of air sampling. At most of the network sites, air samples are collected by volunteers in a cooperative international program. By 1980, the network had expanded to an adequate number of sites to construct accurate global averages. Today, the NOAA global cooperative air sampling network consists of over 50 background land-based sites, where samples are obtained weekly, and three international shipping routes that obtain samples at 5°latitude intervals.

The contribution of long-lived greenhouse gases to climate forcing is well understood by scientists and has been reported through international assessments. Nevertheless, the

D. J. Hofmann, J. H. Butler, T. J. Conway, E. J. Dlugokencky, J. W. Elkins, K. Masarie, S. A. Montzka, R. C. Schnell, and P. Tans